

## Probability based damage detection on a composite fuselage panel based on large data set of guided wave signals

Francisco de Sá Rodrigues<sup>\*</sup>, Ilias N. Giannakeas, Zahra Sharif Khodaei, Ferri M.H. Aliabadi

*Department of Aeronautics, Imperial College London South Kensington Campus, Exhibition Road, SW7 2AZ, London, UK*



### ARTICLE INFO

**Keywords:**

Structural health monitoring  
Guided waves  
Outlier analysis  
Probability of detection (POD)  
BVID detection  
Damage localization

### ABSTRACT

This paper reports on the application and challenges of a guided wave-based structural health monitoring (GWSHM) methodology on an industrial 5 meter-long curved composite fuselage panel, for detecting barely visible impact damage (BVID), based on integrated sensors data. An extensive network consisting of 72 piezoelectric transducers installed on the panel via diagnostic film, a layer including sensors and inkjet printed flexible circuits, that provides uniform bonding quality and repairability. Threshold setting for damage detection is proposed based on statistical distribution of pristine signals, obtained throughout the span of one month. The threshold is determined through an Outlier Analysis and validated through an iterative cross-validation approach. The model validation yields a Gamma distribution with 1.5% false positive rate. A total of 20 impacts at different energies are conducted on the panel for BVID generation and these are respectively categorized based on their location. Methodologies were developed in order to detect, characterize, and localize the BVID generated from the impacts at various locations of the panel. The reliability of the SHM system is quantified by the Probability of Detection for each damage category by computing the damage area with 90% probability and 95% confidence level ( $a_{90 \mid 95}$  values). For damages in the skin and at the foot of the stringer  $a_{90 \mid 95}$  values of 233 mm<sup>2</sup> and 365 mm<sup>2</sup> are, respectively, obtained. Finally, the summary of the experimental work is presented through the detection of all imparted damages.

### 1. Introduction

The increased usage of composites materials in primary and secondary aircraft structures has highlighted the need for optimising their design, maintenance and operation, as well as predictions for their end of life [1,2]. Structural Health Monitoring (SHM) techniques have the potential to provide real-time in-service monitoring of structures to assess their integrity and usage, and to optimise the in-service life of aircraft structures. The aim of SHM is to replace conventional (visual) scheduled-based maintenance techniques to continuously monitor the health of the structure and provide early warning in real-time [2].

Composites are prone to transverse impact events, such as bird strikes, hail, or accidental tool drops during maintenance operations which can result in the generation of Barely Visible Impact Damage (BVID) that is difficult to detect and characterize with existing non-destructive inspection (NDI) techniques. There are various SHM methods that have been investigated and tested extensively not just by researchers but by aircraft manufacturers and operators [3,4] as well. Of

these, the implementation of fibre optic-based sensors is one of proposed techniques which has been extensively tested in aircraft structures, given its high reliability for strain monitoring and impact detection, i.e., Goossens et al. [5] explored the advantages of employing surface mounted fibre Bragg grating (FBG) sensors for monitoring damage evolution at the feet of a stringer on three flat stiffened panels. However, damage assessment through these sensors still yield very restrictive results since only damages in locations in the vicinity of the FBG are correctly localized.

SHM techniques relying on the propagation of ultrasonic guided waves (GWSHM) have been proposed [6] for the detection and localization of BVID on both accessible and inaccessible locations, through the permanent installation of piezoelectric (PZT) sensors on the structure under inspection. Several GWSHM methodologies have been proposed for damage detection however, baseline-based methodologies are the most predominant and reliable techniques since they rely on the comparison between a stage assumed to be damage-free (pristine stage) and other, where damage presence is being inspected. Such analysis requires

\* Corresponding author.

E-mail addresses: [f.rodrigues20@imperial.ac.uk](mailto:f.rodrigues20@imperial.ac.uk) (F. de Sá Rodrigues), [i.giannakeas19@imperial.ac.uk](mailto:i.giannakeas19@imperial.ac.uk) (I.N. Giannakeas), [z.sharif-khodaei@imperial.ac.uk](mailto:z.sharif-khodaei@imperial.ac.uk) (Z. Sharif Khodaei), [m.h.aliabadi@imperial.ac.uk](mailto:m.h.aliabadi@imperial.ac.uk) (F.M.H. Aliabadi).

the employment of damage-sensitive features from the propagating waves associated to, i.e., phase-changes [7,8], signal amplitude variations [9], and time-of-flight [10], for damage detection and localization. However, due to high costs and manufacturing limitations, the validation of GWSHM in large composite structures [8,11] has been addressed to a considerably less extent than smaller structures.

The challenge, however, is to create this database for an actual airframe component, of real size and complexity, replicating conditions of in-service operation. This is one of the fundamental challenges that needs to be resolved before the industrial uptake of SHM technologies as a reliable maintenance strategy by the aeronautics community. The research in this paper has been conducted as part of the CleanSky2 project SHERLOC, where the maturity of the GWSHM technologies and methodologies have been tested and verified starting from a coupon level to element and up to the sub-component level. The application of SHM technologies and methodologies have followed a novel building approach, were the developments started at a coupon level with a large number of integrity and verification tests, followed by mono-stringers and flat stiffened panels [8]. This work extends and enhances the previous research at the lower scales and presents the industrial test level, which is a large, curved fuselage panel. Each level of the building block builds on the previous levels, where larger data sets are available under a wide range of environmental and operational conditions (EOC). As the complexity of the structure increases, it will be more challenging to construct a large library of recorded signals. The novelty of the proposed building block is that the guided wave signal features that are selected for damage detection are material related and therefore, can propagate from coupon to sub-component levels, reducing the number of required tests at larger scales significantly.

Application of SHM to a large-scale sub-component structure requires overcoming various complexities from numerous sources: the development of an acquisition platform capable of performing the actuation and acquisition of signals from large sensor networks with subsequent storage, management, and processing of large datasets; detection of representative impact damage scenarios; optimal sensor placement to circumvent severe attenuation in guided wave propagation, and solve the added weight introduced by the sensor cabling. The proposed SHM system should tackle these drawbacks whilst ensuring that the normal aircraft flight performance is maintained. The MIL-HBK-1823A handbook [12] presents the Probability of Detection (POD) curves as a metric for quantifying the reliability of Non Destructive Evaluation (NDE) techniques. Analogously numerous authors have similarly adopted this index for quantifying the SHM methodologies [7,13,14] as a successful roadmap for future certification SHM in the aeronautical sector. Falchetto et al. [13] insightfully quantify the missing awareness in the SHM community towards these reliability metrics and the need to demonstrate the efficiency provided by SHM systems for damage detection. Furthermore, to build representative POD metrics for SHM systems in aeronautical applications, numerous independent damages must be inspected, representative of impact locations in aircraft components.

In this manuscript, damage detection and localization of multiple individual impacts on the large curved stiffened composite panel, representative of a section of a regional aircraft is presented. The impact events on the structure are divided into four categories: on the skin (from the inside); on the skin (from the outside); at the skin-foot interface (Lip); and at the foot of the stringer to demonstrate various possible damage scenarios that can occur during the service life of an aircraft. A damage detection algorithm is afterwards employed based on the outlier analysis from data collected over the span of one month. The damage propagation from successive impacts at the same location is also monitored through the same methodology allowing for the POD for each damage category to be determined. Subsequent damage localization is calculated through the fusion of classic imaging algorithm. To the authors' knowledge, the available literature for GWSHM mostly focus on smaller structures (particularly CFRP coupons) and easily detected

impact events in highly dense sensor networks, which does not provide enough variability in the data, particularly for POD calculations, and account for the large variability originated in large composite structures, representative of real aircraft sections. Among studies conducted in large structures, the SHM activities developed for the SARISTU project [15] explored the capabilities of guided waves for the detection and localization of single panel impacts performed in a composite wingbox and in smaller unstiffened and stiffened composite panels by relying in path-wise differences to assess the presence of damage. Therefore, an absence in the literature exists on the employment of such large sensor networks in a complex subcomponent aircraft structure which fully account the feature space for the pristine state through guided wave analysis by collecting signals over long time periods, as well as the detection of multiple individual impacts in different locations and with different size, present on the same structure which represent real life scenarios. Furthermore, the large number of impacts performed in each different designed category allows for the respective POD to be obtained for each category rather than grouping the whole detection results in a single damage category.

This manuscript is organized as follows: section 2 details the methodology followed in this work, the design and bonding procedure of the inkjet-printed piezoelectric diagnostic film, as well as the experimental acquisition of guided waves and the post-processing required prior to damage detection; in section 3 the methodology for setting the pristine database and the damage detection threshold, is developed. In Section 4, the multiple damages imparted on the structure are categorized and the respective detection, growth, and localization results for selected few are highlighted. Furthermore, the performance of the current SHM approach is evaluated based on the POD curve for multiple damage categories and various impacts (skin, skin-foot of the stringer interface and foot of the stringer).

## 2. Structural health monitoring of a composite fuselage panel

The sub-component investigated in the work is a 5 meter-long composite curved fuselage panel, representative of a section of a regional aircraft barrel. The panel has 1.67-meter-radius with 6 longitudinal carbon fibre-reinforced polymer (CFRP) stringers, and 7 Aluminium transverse frames. The CFRP stringers were co-cured with the curved panel's skin, whereas the frames were riveted afterwards. The curved panel is divided into multiple bays, each limited transversely by the omega stringers and longitudinally by the frames. The stacking sequences, alongside the thickness for each panel section, are detailed in Table 1. During the test campaign, the panel was supported in a custom-made wooden fixture which allowed the panel to be held in both convex and concave configuration. The panel was designed by the SI&HM group at Imperial College, manufacturing was performed by FIDAMC and tested at Imperial College London, in London, and Element Materials Technology, in Seville.

The challenges related to SHM of a large-scale aircraft structure are both technological and methodological. Therefore, the technological challenges covering sensor installation and data acquisition is introduced first, followed by methodological challenges related to feature extraction, guided wave characteristics and environmental and operational conditions.

### 2.1. Sensor development & installation

Lead Zirconate Titanate (PZT) ceramic disks have been utilized in this research as transducers of guided wave. In particular, DuraAct transducer were selected following a detailed integrity assessment and down selection [16], due to their robustness under EOC. The main source of weight provided by the installation of the SHM system corresponds to the cables soldered to the DuraAct sensors' terminals. Given the panel's dimensions, a large sensor network is required to be installed to provide a broad area of inspection, resulting in significant

**Table 1**

Curved panel sections and respective stacking sequences and design thicknesses.

Panel Radius [mm]	Section	Thickness [mm]	Stacking Sequence
1655	CFRP skin	2.208	[±45/0/90/0] <sub>s</sub>
	Omega stringer	2.208	[±45/0/90/0] <sub>s</sub>

additional weight due to cables. To mitigate this effect, an inkjet printed circuit [17] has been proposed. Inkjet-printed circuits have already been successfully used by our research group previously for cure monitoring and damage detection on adhesively-bonded composites [18], for GWSHM when surface-mounted in flat stiffened panels [8] and when embedded in thick-composite plates [19]. Moreover, this system has been demonstrated to provide significant weight saving features when compared to the cabling solution counterpart [20].

Several parameters have been optimised in this work to increase the quality and reliability of the recorded signals. These parameters include the shape of the tracks, the thickness and width of the tracks, the speed of the printing which is determined by the size of the droplets, and the ink. The conductive tracks were inkjet-printed using a piezoelectric Dimatix DMP 2850 printer with a silver nanoparticle suspension ink. Further details regarding the manufacturing procedure can be found in [18]. To enhance the electrical conductivity of the printed tracks, five layers of silver-based ink with 2 mm width were consecutively printed yielding an average resistance of  $20\Omega$  and  $4\Omega$ , for the longer and shorter tracks, respectively, as illustrated at the bottom of Fig. 2. There is a direct relationship between the length of the tracks and the signal attenuation, therefore, there is an interest in keeping the tracks as short as possible. In addition, the disadvantage of using printed tracks is that they only have partial shielding from the Kapton layer, and there will be interference between the two tracks in the form of crosstalk. To mitigate the large possible crosstalk between the actuator and sensing channels, two transducers are positioned on each diagnostic film, with their connectors placed on the opposite sides. In addition, the geometry of the tracks are optimised to result in short length, no sharp edges and as far from each other as possible to reduce the interference, see Fig. 2 for the representation of the assembly, which demonstrates the diagnostic film (flipped for demonstration purposes only) without cabling, prior bonding.

The DuraAct PZT sensors were then connected to the printed wires using a two-part silver-loaded epoxy adhesive (RS Pro Liquid Adhesive), cured at 85 °C for 30 minutes and surface-mounted connectors (Tokyo Measuring Instruments Lab.) were used to connect the coaxial cables to the printed wires. The printed sensors were bonded to the curved panel's surface using a thermoplastic adhesive film which has been previously demonstrated to be a repeatable and reliable bonding procedure for piezoelectric sensors in different structures [21]. Due to the size of the panel, the curing of the thermoplastic film was carried out using a portable Anita Hot Bonder repair console which ensured a proper temperature cycle, and a separate pump ensured the required pressure during curing.

Each bay was sensorized using 2 printed diagnostic films (4 PZT sensors in total) to avoid the exponential attenuation of Lamb waves over long distances [22]. Moreover, a wide area-coverage was desirable for the current testing campaign. Hence, a total of 36 diagnostic films were bonded throughout the 3 inner rows of the panel leading to network of 72 PZT sensors. The full sensorization of the curved panel is illustrated in Fig. 3 (also highlighted in Fig. 1).

After the installation procedure is finalized, the bonding integrity was inspected through individual Electro-Mechanical Impedance (EMI) Analysis using a Sinephase Impedance Analyzer 2097k to ensure proper transmission of the signals, and that the cabling was not damaged. EMI-based techniques have also provided [23] a reliable method for damage detection in close vicinity to the sensors. The absence of defects in the cabling and proper bonding to the structures are assumed when the real part of the impedance presented a frequency shift on the first peak, compared to the free-sensor EMI response (from around 200 kHz to approximately 250 kHz). Fig. 4 illustrates the conductance results (Admittance's real component) of the EMI analysis for 12 bonded individual PZT sensors and for a free PZT sensor. Furthermore, Fig. 5 summarizes the EMI's conductance component magnitude and frequency results for the first peak in all the 72 bonded PZT sensors. Analysis of both Figs. 4 and 5 shows a consistent shift on the first peak frequency between the bonded and free sensor EMI and a decrease in the Conductance magnitude.

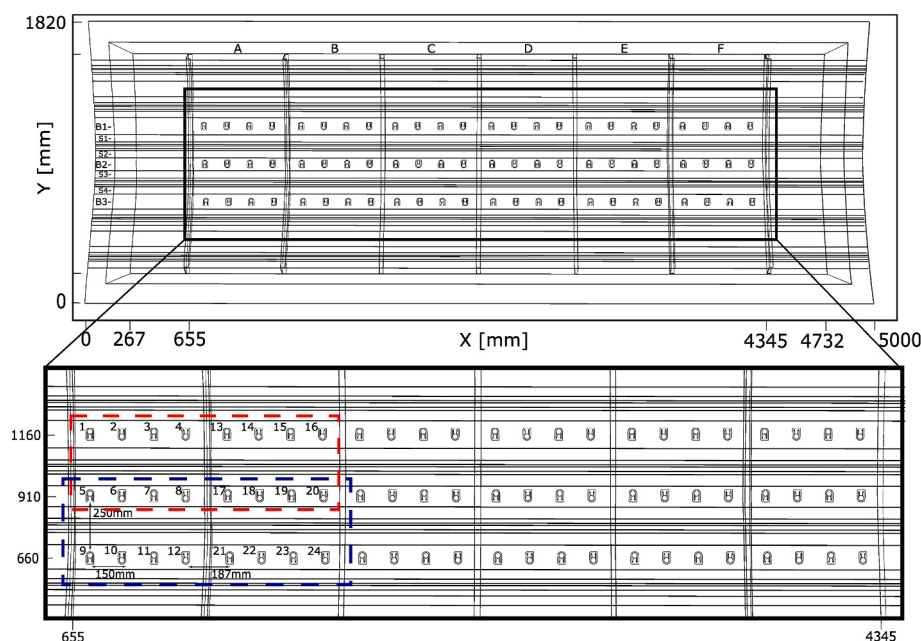


**Fig. 1.** Curved panel schematic with sensor locations and highlight in the sensorized bays and two examples of acquisition subnetworks in red and blue. (For interpretation of the references to color in this figure legend, the reader is referred to the Web version of this article.)



**Fig. 2.** Diagnostic film detail with bonded DuraAct PZT sensors and respective position in multiple bays of the curved panel.



**Fig. 3.** Curved panel full sensorization.

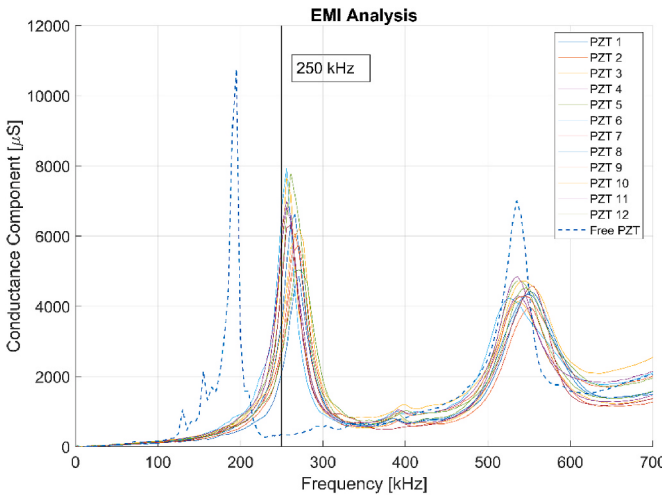


**Fig. 4.** Conductance component of EMI for 12 bonded PZTs and free PZT response.

## 2.2. Guided wave acquisition

The challenges of GWSHM for monitoring large scale structures in service under EOC are multiple, the three most significant ones are:

- There are multiple damage scenarios in various location that can occur in a stiffened panel which will have very different guided

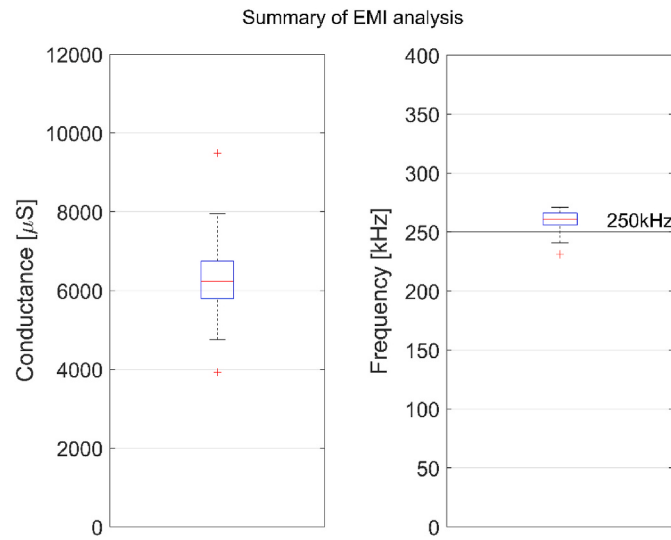


**Fig. 5.** Summary of the EMI results for the 72 bonded PZTs at the 1st resonance peak.

wave-damage interaction and therefore will result in different optimum excitation signal (waveform and frequency) for damage detection and characterisation. For example, debonding between skin/stiffener will have different features compared to through thickness damage.

- Different wave modes (symmetric or anti-symmetric) will have different attenuation coefficients, as well as different sensitivities to environmental variabilities such as temperature, which means that for different location and complexities of the sensorised parts, there will be different optimum frequencies for monitoring the structure, in particular for composite structures.
- Since the most reliable GWSHM methodologies for damage detection are baseline methods, this will result in a need for a large database of signals to be recorded in a pristine state first under a large range of EOC, followed by the current state signals recorded and post-processed.

Therefore, to handle such large dataset that is required to create a database of pristine signals recorded under various conditions, including multiple frequency response not only technological innovation in data acquisition hardware and software is required, but also methodological advancement is necessary to optimise the data acquisition, handling and storage.

The development of an SHM acquisition platform is thoroughly detailed in [24]. For this work, this system was expanded to account for the larger sensor network and the multiple actuator-sensor paths combinations. The improvement to the initial platform and the final assembly system can be found in [25].

### 2.2.1. Guided wave actuation signal

The actuation signal consisted of a linear chirp with an initial frequency  $f_0 = 10$  kHz, a final frequency  $f_1 = 600$  kHz, and a signal peak-to-peak amplitude  $V_{pp} = 24$ V. The actuation signal is given by the expression in equation (1). The guided waves generated by this actuation signal were acquired in a round-robin configuration.

$$V(t) = V[H(t) - H(t-T)] \sin\left(2\pi\left[f_0 t + \frac{f_1 - f_0}{2T} t^2\right]\right), \quad (1)$$

where  $T$  is the chirp signal duration, here considered as 200μs. The experiment's signal-to-noise ratio was improved by performing 10 consecutive measurements each time and averaging the signals. The linear chirp excitation allowed for a wide range of desired frequencies to

be excited at once. However, to obtain an individual guided wave mode, an optimal unique frequency must be excited. Therefore, during the post-processing phase, the signals resulting from the linear chirp excitation were deconstructed to generate the individual 5-cycle Hanning windowed toneburst signals with desired central frequency [26]. The ability to reconstruct any desired single-frequency toneburst response from the recorded chirp signal resulted in significant acquisition time savings and optimal data storage, whilst generating the same signal as with a toneburst actuation. The fundamental antisymmetric and symmetric wave modes, A0 and S0, respectively, were determined to have an optimal actuation frequency at 50 kHz and 250 kHz, respectively.

To account for eventual temperature variations in separate acquisition times the acquisition platform incorporated a temperature acquisition unit which registered the temperature values during the acquisition measurement.

### 2.3. Damage sensitive features

The identification of the damage presence will be performed based on the comparison between the signals acquired at a reference pristine state, and another state where the damage presence is being inspected. Therefore, the damage index (DI) for actuator-sensor pair,  $j$ , is given by,

$$DI_j = 1 - \left[ \frac{\text{cov}(s_j^{\text{ref}}(t)w(T), s_j(t)w(T))}{\sigma(s_j^{\text{ref}}(t)w(T))\sigma(s_j(t)w(T))} \right] T = [t_1, t_2], \quad (2)$$

where  $s_j^{\text{ref}}$  and  $s_j$  correspond to the baseline (damage-free), and current signals, respectively, and the term in brackets is the Pearson's correlation coefficient. For this operation, a time window  $w(T)$  was applied to restrict the analysis to the A0 mode's first wave packet, with path-dependent group velocity  $v_g$ , where for a sensor pair with distance  $d$ ,  $t_1 = \frac{d}{v_g}$  and  $t_2 = t_1 + n/f_c \times 1.1$ . The inclusion of a time window allowed for events which purely affect the first wave packet to be considered in the analysis like phase shifts, attenuations and mode conversions arising from interaction with the damage. Following the procedure adopted in [8] for damage detection using guided wave signals over similar paths as those considered in the current work, a constant factor 1.1 is considered to ensure inclusion of the full wave-packet due to dispersion effects. However, to improve future windowing processes, path dependent

time-windows could be considered in the analysis. The direction dependence of the group velocity has been considered for computing each path's time window.

The damage index relying on the correlation coefficient was observed to yield higher sensitivity to damage presence whilst minimizing the indices for the remaining unaffected paths by attaching artificial damages to the panel's surface. Other explored damage indices involved the ratio between the residual ( $s_j^{\text{ref}} - s_j$ ) and the baseline signals [9] and the root mean square indices [27].

### 2.4. Sensor grouping

The adoption of a SHM Building Block (BB) approach for application to aircrafts has been introduced by Yue et al. [8] similar to the approach employed for mechanical certification of aircraft components, where the extensive test campaign on a full-scale aircraft component proves to be financially unaffordable to fulfil all the required demands from the authorities. Hence, an extensive testing and analysis campaign is carried out in smaller representative structures, starting from small coupons all the way to aircraft component, while propagating the required properties towards the upper BB levels. For the SHM BB approach, a large test campaign was performed on flat coupon plates (with the same prepreg material) representative of the panel's skin where angular group velocity profiles were extracted. Afterwards, a skin reinforcement was added in the Element level which allowed for the attenuation profile to be accounted and the influence in the temperature compensation profile and include impact scenarios at the foot of the reinforcement. However, in order to maintain the validity of the information propagated from different BB structures, the employed sensor network must be analogous between the levels.

The full inspection of the stiffened panel required grouping of the sensors to provide maximum coverage area for damage detection and localization, whilst respecting the attenuation profile of the signals, the limitations of the acquisition unit (number of channels) and the amount of stored data. Therefore, the total 72 sensor network was divided into 10 smaller overlapping subnetworks each with 16 sensors (as illustrated in Fig. 1) which allowed for an optimum area coverage, as well as balance the post-processing time and amount of data per acquisition. However, for large propagating distances between sensors, and which

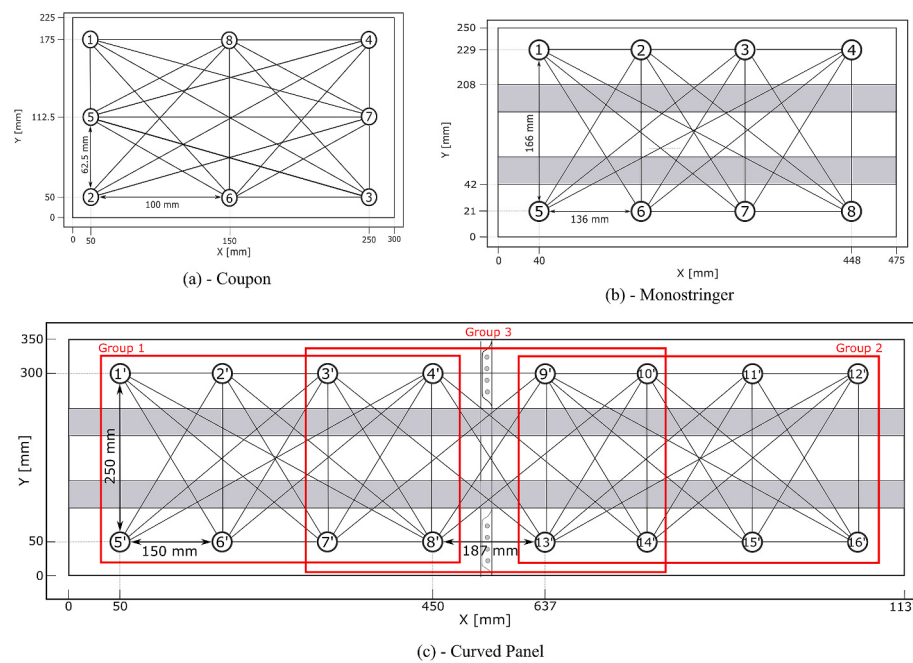


**Fig. 6.** Sensor pair grouping based for different building block levels (Coupon, Element and Sub-Component).

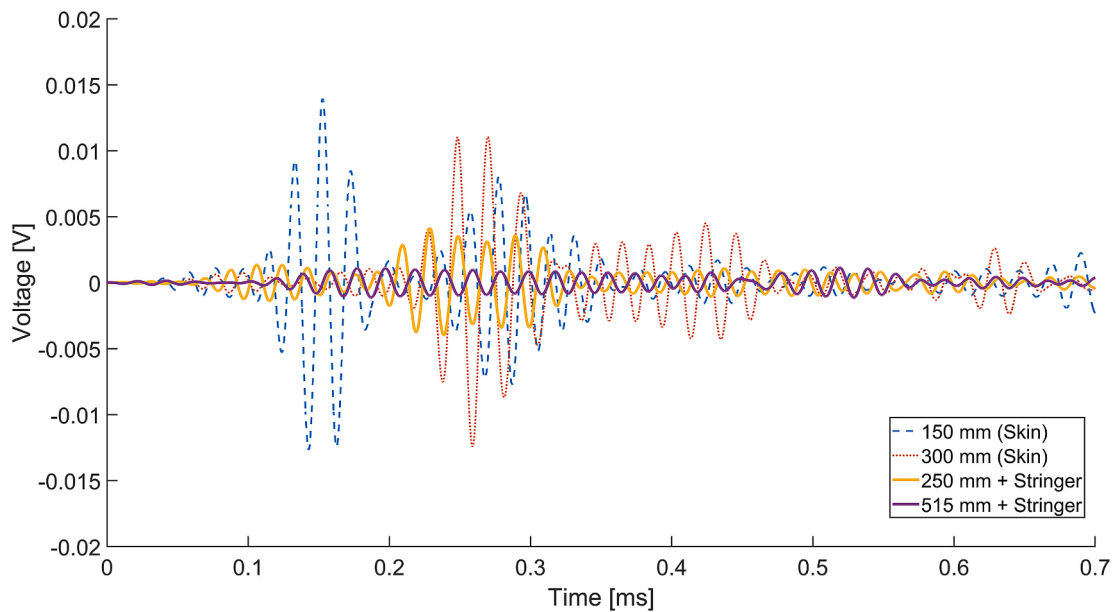


Fig. 7. Wave propagation for different actuator-sensor path distances.

simultaneously cross the stringers the resulting signals are unusable given the high amplitude attenuation and stringer effects. Given the extensive experimental campaign previously carried out in the lower BB levels, the group of 8 sensors can be considered as a repeating pattern from the monostringer level to the curved panel level. Although each subnetwork of 16 sensors can be divided into 2 groups of 8 sensors, this would generate a blind spot at the location of the vertical frame. To mitigate this, a third group is introduced (group 3) that covers this region. The groups of sensors are illustrated in Fig. 6. The current 8 sensor configuration included signals with good signal-to-noise ratios and discarded actuator-sensor pairs with signals of the same amplitude as the environmental noise. Following the proposed path eligible criteria [8, 28], the acquisition sensor network is segmented into three smaller subnetworks ( $i = 1, 2$  and  $3$ ), each with 8 sensors, to ensure the same monitoring area as the original network. The groups of sensors are illustrated in Fig. 6, where the number of eligible pairs for each group,  $n_i$ , is 44, 44 and 40, respectively.

The post-processing phase of the acquired signals involves computing the pair-wise DI for each grouping,  $Dl_{Gi}$ , where the subscript  $G_i$  corresponds to the grouping index and  $i = [1, 2, 3]$ . Hence, the size of the DI grouping arrays  $Dl_{Gi}$  is equal to the corresponding grouping's number of actuator-sensor pairs ( $[n_1, n_2, n_3]$ ). The mean and standard deviation for each grouping's DI array, with  $n_i$  actuator – sensor pairs, is then calculated and given using equations (3) and (4). These statistical features are here considered as damage features and are stored for posterior usage for calculating the damage detection threshold.

$$\mu_{Dl_{Gi}} = \frac{\sum_{j=1}^{n_i} Dl_j}{n_i}, \quad (3)$$

$$\sigma_{Dl_{Gi}} = \sqrt{\frac{\sum_{j=1}^{n_i} (Dl_j - \mu_{Dl_{Gi}})^2}{n_i - 1}}, \quad (4)$$

The presence of temperature variations between signal acquisition are expected to introduce non-damage related variations in the signals and, consequently in the damage detection features and influence the threshold definition, however, given the relatively controlled laboratory environment in which the current experiments were conducted. Such variations are considered part of the experimental signal uncertainty. Furthermore, the presence of crosstalk arising from

electromagnetic interference between the inkjet printed track was investigated by inspecting the initial portion for each signal path present in the respective schematic of Fig. 6. This analysis comprised 11960 individual signal paths where only two instances presented an amplitude at the early portion of the signal (between 0 and 0.1 ms) which was substantially higher than the maximum of the remaining signal. However, the application of a time-window on the damage detection phase proved to avoid any impacts from this random effect to the current analysis.

## 2.5. Guided wave characteristics

In thin plates, guided waves can be divided into symmetric and antisymmetric waves, each consisting of infinite wave modes. However, conventional guided wave modes for SHM purposes are restricted to low-frequency modes, namely S0 [9,29] and A0 [8,30], to avoid complexities arising from the signal's multi-modal mixture. For curved structures, the cylindrical modes: torsional [31], flexural, and longitudinal wave modes are obtained rather than the aforementioned ones. For these structures, Gazis [32,33] developed the analytical expressions required for analysing the wave propagation. Moreover, the modal analysis of hollow cylindrical guided waves by Nishino et al. [34] presented the resemblances for the fundamental axisymmetric longitudinal wave modes L(0,1) and L(0,2), and the thin-plate modes A0 and S0, respectively. For the current curved panel, the respective values detailed in Table 1 provide a diameter-to-thickness ratio which allows the guided waves propagating in the current curved panel to be treated as the ones obtained in a flat panel. This work focused on the employment of the A0 wave mode during the damage assessment framework given the results reported in Refs. [7,35], where the fundamental antisymmetric wave modes higher sensitivity to BVID detection and localization was demonstrated in comparison to the in-plane S0 modes. Additionally, the reconstruction of the toneburst signals for higher frequencies resulted in reduced signal-to-noise ratios which compromise the current analysis.

Some of the concerns regarding the implementation of an SHM system in large aircraft have been addressed so far, particularly the ones related to weight increase, sensor installation methodology, development of an acquisition platform and efficient acquisition strategy for large sensor networks. However, from a postprocessing perspective, the large size of the current stiffened panel and the respective size of the sensor network arises several difficulties. For the damage metrics

calculation, the accurate time window correspondent to the  $A_0$  wave mode must be selected. Given the anisotropic mechanical properties of the panel, the wave mode velocity is variable with the propagation angle and the wave is subjected to the attenuation and reflections at the stringer's interface. Hence, selecting the accurate time of arrival (TOA) for some actuator-sensor paths proves to be difficult using the methodologies used in lower levels of the BB [36] as observed in Fig. 7. Here, the actuator sensor path distances in the legend corresponds to the ones from Fig. 6, where the paths with distances of 150 and 300 mm correspond to the wave propagation between sensors in the same bay, i.e., paths 1–2 and 1–3, respectively. Even though the latter is not considered during the postprocessing analysis, the similar propagation distances illustrate the attenuation from the stringer for other similarly distanced actuators and sensors. The paths with distance of 250 mm correspond to the wave propagation for actuator and sensors in two different bays with a relative angle of  $90^\circ$  separated by a longitudinal CFRP. Finally, the plot with distance of 515 mm corresponds to the propagation of a signal over maximum distance separating an actuator and sensor in the subnetwork. In Fig. 7 the high attenuation from the stringer is demonstrated, where for particularly large distances, results in very low signal amplitude. The signals illustrated in Fig. 7 correspond to the reconstructed 50 kHz toneburst signals from the original chirp excitation results following the framework detailed in [26].

This effect is more evident when calculating the TOA for all the transducer paths included in the curved panel schematic in Fig. 6. Repeating this calculation for all the 10 acquisition subnetworks using the maximum-likelihood method [36] and ordering the results according to the actuator-sensor distances yields the results in Fig. 8 (a). Particularly for the signals associated with actuator-sensor paths crossing the CFRP stringer, the TOA computing was filtered using a maximum ceiling for the wave's group velocity correspondent to the numerical group velocity calculation using the Semi-Analytical Finite Element method (SAFE) [37]. This was a requirement since for these paths, the TOA corresponds to the S0 wave mode since both modes have similar amplitudes due to different attenuation factors from the stringer. Nonetheless, analysis of Fig. 8 (a) clearly shows the higher variability on the TOA calculation for higher actuator-sensor distances given the lower signal-to-noise ratio highlighted in Fig. 8 (b). Therefore, a more detailed inspection to the highest actuator-sensor paths (paths 1–8, 4–5, 9–16, 12–13) was conducted for all ten 16 sensor-subnetworks where the absence of any significant changes between consecutive signals

validated the employment of these paths in the analysis.

Given the predominant importance of the TOA variable for the damage detection metric given in equation (2), the mode of the TOA computed for the actuator-sensor paths distances in Fig. 6 was used for computing the damage detection window in equation (2).

### 3. Damage detectability threshold

The reliable distinction between undamaged and damaged states requires a robust threshold to be defined. Numerous methods have been proposed for defining the damage detectability threshold, the outlier analysis proposed by Yue et al. [8] for the building block approach is utilized in this work.

For univariate data, outlier analysis simply states if a given observation falls out of both ends of a data set, i.e.  $z_\varphi = \frac{|x_\varphi - \mu|}{\sigma}$ , where  $x_\varphi$  is the potential outlier, and  $\mu$  and  $\sigma$  are the sample's mean and standard deviation, respectively. Here the sample corresponds to the pair-wise damage indices array  $DI$ , from equation (2), and the respective mean ( $\mu_{DI}$ ) and standard deviation ( $\sigma_{DI}$ ) follow equations (3) and (4), respectively. For multivariate data (like the present application), this translates into a more complex case where the discordancy is given by the Mahalanobis' squared distance,

$$Mahal_n^2 = (\{x\}_n - \{\bar{x}\})^T [S]^{-1} (\{x\}_n - \{\bar{x}\}), \quad (5)$$

where  $\{x\}_n = [\mu_{DI}, \sigma_{DI}]$  is the potential outlier array,  $\{\bar{x}\}$  is the mean of the pristine database samples and  $[S]$  is the sample covariance matrix.

For setting the threshold for damage detection, guided waves were acquired for all the panel's 16-sensor subsections (Fig. 1) through the span of 1 month and a maximum temperature difference ( $\Delta T$ ) between signals of  $\pm 4^\circ C$  was registered. Furthermore, the effect of the boundary conditions was considered by positioning the panel in 2 different configurations, convex and concave orientations. Given the relative controlled environment in the lab the temperature variations registered using the experimental setup were considered as part of the measurement uncertainty in order to register the variations in the environmental conditions during signal acquisition over a considerable time span. Analogously, the current analysis accounts for the path-dependent signal variations within each grouping's detection features during the collection of the pristine data signals which are accounted for in the damage detection threshold.

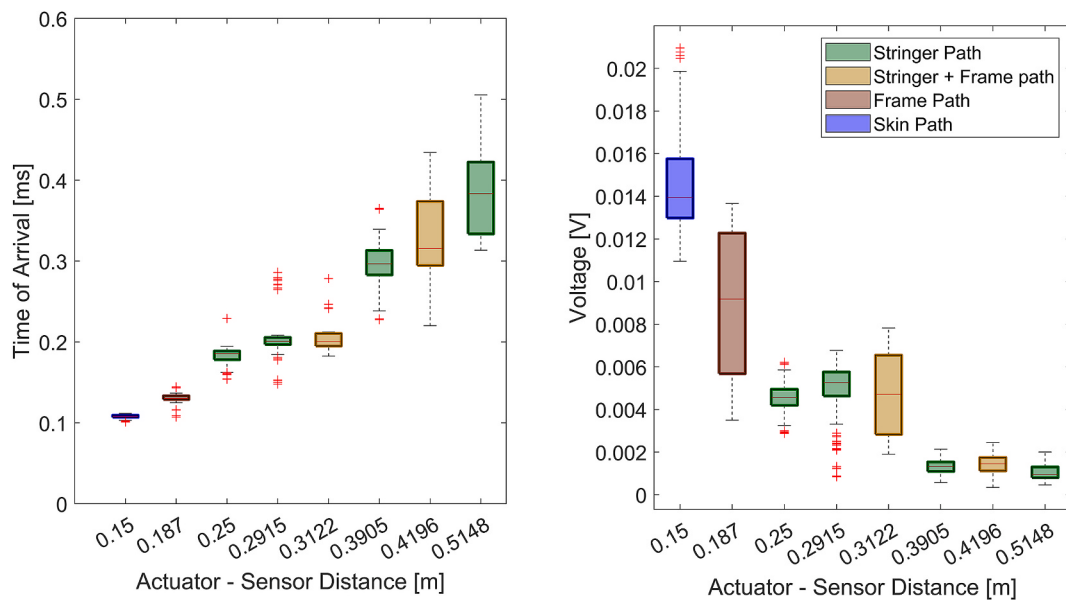


Fig. 8. A0 wave mode TOA (a) and signal amplitude (b) for all actuator-sensor path distances.

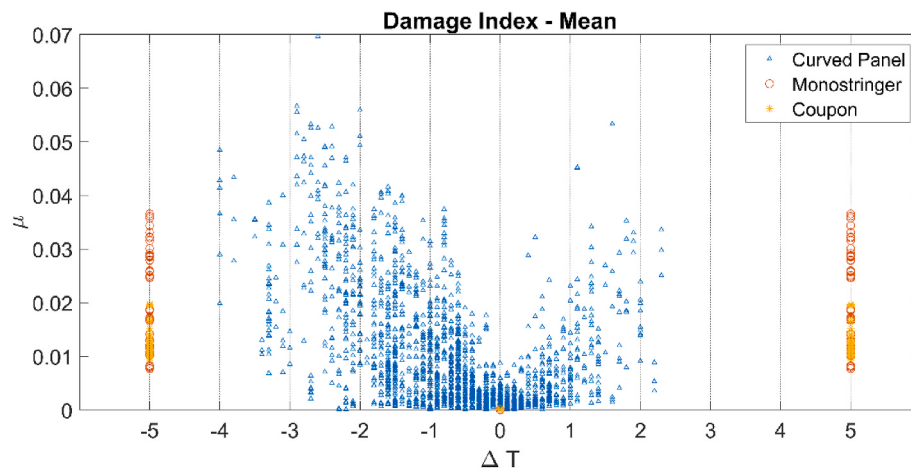


Fig. 9. Mean of the DI array in different Building Block levels.

The signals for each eligible actuator-sensor pair were compared following equation (2) in each of the 3 groupings of 8 sensors discussed in section 2.4, resulting in three  $DI$  arrays with lengths  $(l_1, l_2, l_3) = (44, 44, 40)$ , where subscripts 1, 2 and 3 correspond to the subsection group indices. For each  $DI$  array, the mean ( $\mu_{DI_{Gi}}$ ) and standard deviation ( $\sigma_{DI_{Gi}}$ ) values were computed, yielding three ( $\mu_{DI_{Gi}}, \sigma_{DI_{Gi}}$ ) pairs for each signal comparison. This procedure is repeated for all allowable signal permutations resulting in an extensive array of damage feature pairs of 1,974 data points.

The reported validation process was individually applied to data collected from all the available BB levels (Coupon, Element, and Sub-Component), represented in Fig. 6. The levels presented similar stacking sequences and manufacturing methods, where the data from the coupon and monostringers corresponds to the one taken for the nearest temperature difference as the current dataset ( $\pm 5^{\circ}\text{C}$ ). The mean and standard deviation results of the damage index array ( $\mu_{DI_{Gi}}$  and  $\sigma_{DI_{Gi}}$ ) for the three building block levels are, respectively, illustrated in Figs. 9 and 10. Analysis of the overall mean results between each building block levels show a consistent increase as one progresses through the BB, though this increase is slightly more significant in the curved panel given the larger amount of collected data and respective variability whilst the coupon and monostringer signals were collected in an environmental chamber of much smaller dimensions. This uncertainty in the environmental effects is more pronounced when analysing the results for the standard deviation which highlight the uncertainty from the random environmental effects alongside considering similar number of paths but

of higher propagation distances between sensors and simultaneous crossing of longitudinal stringers which are absent in the lower-level structures. Hence, this uncertainty is translated in the higher coefficient of variation (ratio between standard deviation and mean) obtained in the curved panel groupings DI values for close mean values obtained in the monostringer structure. Though the chamber provides higher control capabilities, the inherent variability associated to the random environmental effects on the damage detection features for the sub-component structure is noticeably higher than those associated to smaller components given the reduced dimensions and smaller signal variability.

Upon analysing the pristine signal database for the curved panel, the signals with temperature differences ( $\Delta T$ ) closer to  $0^{\circ}$  were obtained at a higher rate than the ones with larger temperature differences. However, a direct trend between increase temperature differences and the larger feature values ( $\mu_{DI_{Gi}}, \sigma_{DI_{Gi}}$ ) was observed. Hence, when building the training database for computing the detection threshold, both higher and lower temperature differences must be simultaneously considered. Hence, the traditional K-Fold and Holdout validation methods are insufficient here since the total database cannot be randomly equally split into training and testing sets and these methods would force the threshold to heavily consider data from signals close to small temperature difference whereas the data associated to higher temperature variations would be treated as potential outliers. Though this would improve damage detection by allowing for smaller damages to be detected, when considering pristine signals with large temperature dif-

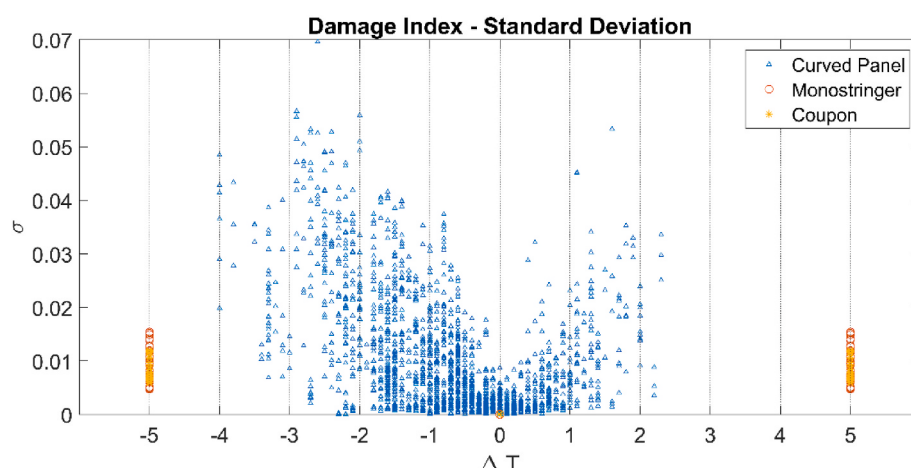
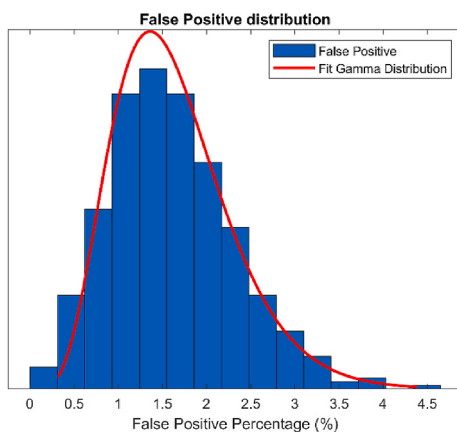
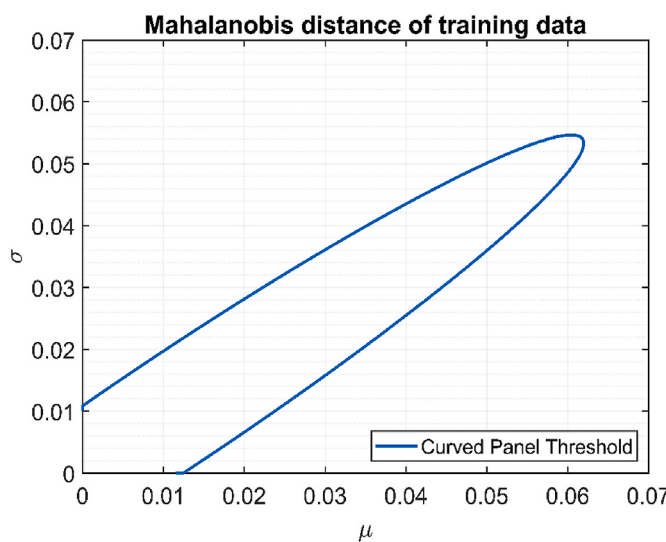


Fig. 10. Standard deviation of the DI array in different Building Block levels.



**Fig. 11.** False Positive percentage distribution from cross-validation procedure for the curved stiffened panel.



**Fig. 12.** Damage detection threshold for the curved panel.

ferences, the resulting  $(\mu_{DI_{Gi}}, \sigma_{DI_{Gi}})$  pairs would be indicating false positives. Hence, for validating the threshold model, an iterative stratified cross validation process was used where the temperature difference

range was sequentially divided into 10 equally spaced ranges and, for each range, 10 random  $(\mu_{DI_{Gi}}, \sigma_{DI_{Gi}})$  pairs were extracted for training the threshold model, whereas the remaining available data in each  $\Delta T$  interval was used for testing. In each iteration, the threshold is defined as the probability that a signal is misclassified as damage. The threshold is computed using a chi-squared distribution with 2 degrees of freedom for the training dataset's Mahalanobis distance where the misclassification probability is given as 99.9% to reduce any false positives. The pristine state was assumed to correspond to any  $(\mu_{DI_{Gi}}, \sigma_{DI_{Gi}})$  combination comprised by the boundary defined by the aforementioned distribution. Finally, the threshold model validation was performed by evaluating the False Positive (FP) values for the testing dataset. Let the parameter  $d$  be a state indicator where  $d = 0$  and  $d = 1$  represent absence and presence of damage, respectively. Moreover, considering  $p$  as the parameter indicating the true health state of the structure, the FP rate is given by the confusion matrix section where:

$$FP = P(d = 1 | p = 0). \quad (6)$$

The iterative procedure for the model validation yielded an occurrence array for the testing dataset's FP percentage with mode equal to 1.5% and approximated through a gamma distribution (FP). The occurrence distribution and corresponding gamma approximation are illustrated in Fig. 11. The FP values obtained from the threshold model test provide an acceptable false positive rate for damage detection considering the amount and variability of the environmental conditions comprised in the training data.

The threshold line with the FP percentage closest to the mode of the fitted distribution was used for the following sections and is illustrated in Fig. 12. Damage is then considered to be present if the damage detection features from equation (2), are placed outside the threshold detection curve.

#### 4. Impact description

Impacts on the curved panel were performed in two distinct environments, one at Imperial College London using a PCB Piezotronics Hammer [38] with a custom-made steel tip of 20 mm diameter, and at Element Materials Technology, in Seville, using a drop tower with a similar geometry tip. The impact energy was dependent on the panel thickness at the location of impact, given in Table 1. Hence, for impacts on the skin and the foot of the stringer, an energy of 25J and 35J was performed, respectively, corresponding to a general tool drops [2].

Table 2 details and categorizes the numerous impact events on the stiffened curved panel. The table comprises the panel's transverse row

**Table 2**  
Impact Scenarios tested.

Damage category	ID	Impact Side	Impact Instruments	Impact Energy (J)	Damage Area	Coordinates
Skin Outside	A - B1	Concave	Hammer	25	150   248   656	(0.430; 0.550)
	A - B3				138   645	(0.130; 0.050)
	E - B2				270	(3.538; 0.300)
	F - B3				270   450	(3.725; 0.550)
Skin Inside	B - B2	Convex	Hammer	25	289   423	(0.767; 0.300)
	D - B2				257   480	(2.7510; 0.300)
	E - B2				255   440	(3.388; 0.300)
	F - B1	Convex	Hammer	25	456	(3.875; 0.300)
	F - B3				380	(4.175; 0.550)
	B-Lip1				160   387	(1.070; 0.500)
Skin-Foot Interface (Lip)	B-Lip3	Concave	Hammer	25	220	(1.070; 0.100)
	E-Lip1	Convex			220   360	(3.238; 0.500)
	E-Lip3	Convex			180   375	(3.238; 0.100)
	B-S2	Convex	Hammer	35	288   722	(0.917; 0.370)
Stringer's Foot	C-S2				254   568	(1.964; 0.370)
	C-S4				149   541	(2.114; 0.120)
	D-S1				580	(2.751; 0.480)
	D-S3				545	(2.976; 0.230)
	G-S1	Convex	Drop Tower	35	188   297   540	(2.114; 0.480)
	G-S3				570	(2.339; 0.230)

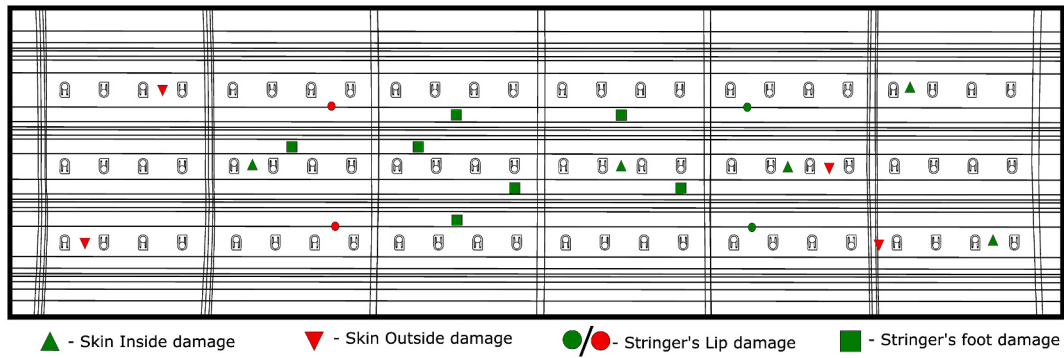


**Fig. 13.** Schematic illustration of the damage locations.

number, impact side (inside or outside), impact energy, the damage area and respective coordinates on the panel's global system. The damage locations and respective category can be found illustrated in Fig. 13.

#### 4.1. Damage detection

Once the threshold is set, one can proceed to the detection of damage events by comparing the grouping's pair-wise damage index mean and standard deviation ( $\mu_{DL_{Gi}}, \sigma_{DL_{Gi}}$ ). Naturally, when damage is present in a group overlap, i.e. between sensors 3, 4, 7 and 8 for groups 1 and 3, and 9, 10, 13 and 14 for groups 2 and 3, two of the three predictor pairs are highlighted. Fig. 14 shows the location of three separate damage categories (B-B2, B-Lip1 and C-S2) from Table 2, with their respective c-

scans and enclosed areas, and the detection results through the outlier analysis. The ultrasound c-scan images were obtained using a portable DolphiCam device (supplied by DolphiTech) after each drop-weight impact was performed. In Fig. 14, damage number 1 corresponds to delaminations resulting from 2 sequential 25J impacts on the panel's skin using a PCB hammer. Damage number 2 was performed in the same conditions as damage 1 but only one impact was performed at 25J and in the interface between skin and the foot of the stringer. Damage number 3 corresponds to an impact at 35J performed on the foot of the stringer with the same tool.

Analysis of the detection results presented Fig. 14 (a), (b) and (c) reinforce the benefits of using the outlier analysis for damage detection given the success in detecting all the existing damages solely in the

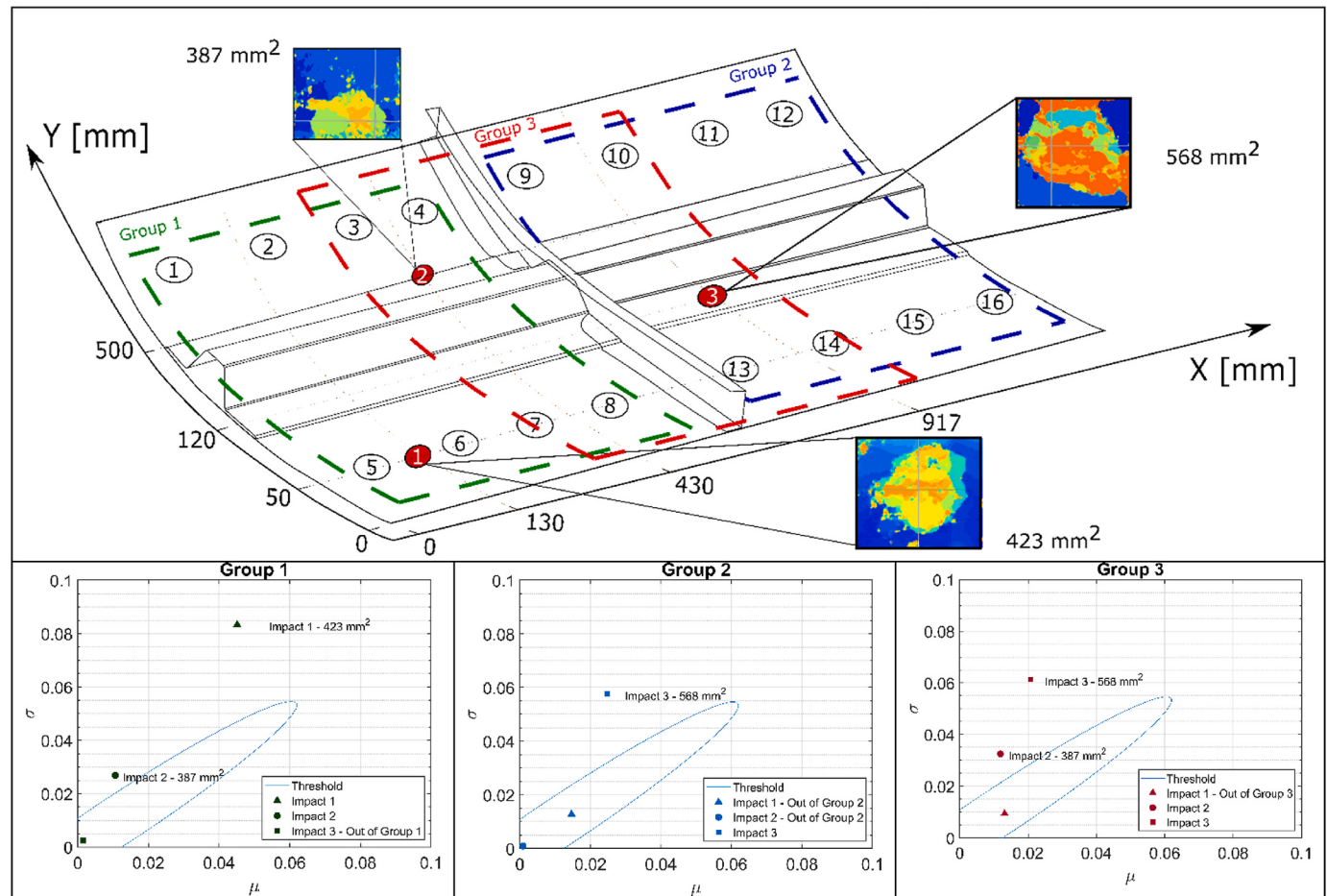


**Fig. 14.** Damage location in the panel and respective damage detection results.

sensor group to which they are circumscribed, i.e. damage in the skin (location 1) is only detected in group 1, whereas the damage at the foot's lip (location 2) is detected by both groups 1 and 3, and the damage at the foot of the stringer (damage 3) is detected by both groups 2 and 3. Moreover, the inspection of overlapping groups allows a preliminary damage localization since the mutual regions between sensor groupings restricts the damage localization to the area comprised by 4 sensors. Finally, a closer inspection to the  $(\mu_{DI_{Gi}}, \sigma_{DI_{Gi}})$  results in Fig. 14 clearly implies that its values are not purely proportional to the damaged area, but also dependent on the damage location, severity, and the number of affected paths as will be demonstrated in the following section.

#### 4.2. Damage severity detection

In this section, the current observable influences on the damage detection features are discussed. The impact location effect on the damage detection has been demonstrated to be of great influence given the statistical effect from the outliers. The current limitations on the detailed inspection do not allow the distinction on the influence from the matrix/fibre damage magnitude hence, only the damage area/severity correlation given by the respective c-scan NDI (estimated from the

images obtained through the portable DolphiCam instrument) is possible. Repeated drop-weight impacts at a given location were performed to increase the severity for some of the impacts at every damage category in Table 2.

In this section the relationship between the detection features ( $\mu_{DI_{Gi}}$ ,  $\sigma_{DI_{Gi}}$ ) and the damage severity has been investigated in order to not only assess the propagation of damages through repeating impacts at the same location, but also provide a framework on how to reliably set a detectability threshold for different damage types. From the results reported in Fig. 14 it can be observed that the detectable damage size for damage at the foot of stringer is different than damage in the bay or under the stiffener hat. Therefore, in analysing the PoD and reliability of any SHM system, the minimum detectable damage size needs to be investigated for all possible damage types, as well as severity. For increasing the damage severity in this work repeating impacts have been performed at the same location, which further increases the differences to the signals obtained at the pristine stage, both in amplitude and in the signals' TOA. Hence, the outlier analysis is again proposed as a way of highlighting damage severity from an assumed pristine state.

The results reported in Fig. 15 (a) and (b) highlight the importance of closely monitoring the propagation of existing damages, particularly for

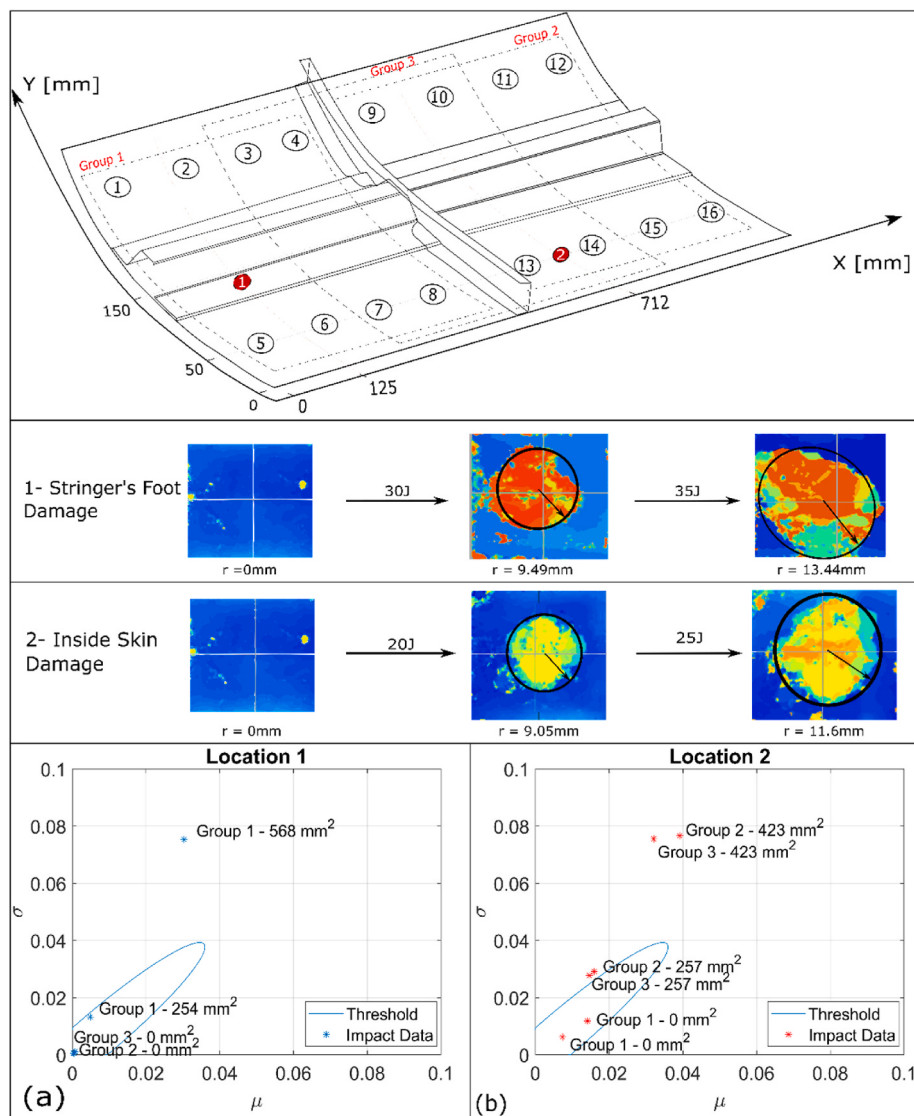


**Fig. 15.** Damage growth monitoring for: (a) Impact at the foot of the stringer; and (b) impact on the skin (inside).

the damage located at the foot of the stringer (damage 1). For this case, the first impact produced a damage with a 9.5 mm radius which is slightly larger than in the case of damage 2, where damage presence is easily identifiable. However, whilst the latter is successfully detected, Fig. 15 (b), the first impact at location 1 isn't, Fig. 15 (a), even though the severities are similar (multiple delaminations at different depths). Hence, the aforementioned results reaffirm the results obtained in Fig. 14, where the sensitivity of the proposed methodology is dependent not only on the damage's size and severity but the impact location as well, given the amount of sensor paths highlighting the damage presence. Nonetheless, by reimpacting the same location, the growth of damage 1 to a delamination with a radius of 13.4 mm ( $568 \text{ mm}^2$ ) is detected through the proposed methodology.

#### 4.3. Impact from inside vs outside of the panel

The current drop-weight setup only allowed for impacts at different sides of the panel at the skin level to be performed which provided for detailed inspection on the influence of the impact side for damages with similar severity and size. The damage size generated from transverse impacts performed at a given energy is dependent on the local material properties, namely strength properties and damping, which influence the indentation occurring. Hence, locations with higher damping and resistance to deformation will present larger damages. The variability associated to manufacturing of fibre-reinforced polymers leads to

similar uncertainties in the damage size which highlights the benefits of performing numerous impacts to obtain a good statistical distribution for guided wave analysis. Here the impacts performed in locations corresponding to ID's E-B2 and F-B3, on the concave side and, B-B2 and D-B2, on the convex side, will be analysed given the similar obtained damage sizes (estimated from the portable c-scan instrument) obtained for the first impact damage.

The signals, given by the  $A_0$  dominated wave mode, for the actuator-sensor path where the damage is located were solely inspected since these correspond to the ones where damage presence should be mostly evidenced. These results are plotted in Fig. 16. Additionally, the  $S_0$  dominated signals were inspected by reconstructing the chirp signal response to a 250 kHz Hanning windowed toneburst and are presented for the signals taken before and after each respective damage in Fig. 17. As evidenced by the results in these figures, the out-of-plane dominated wave modes evidence the presence of damage more pronouncedly to the respective in-plane counterparts.

Quantification of the signal differences was performed by computing the correlation coefficients for these signals using equation (2), for the time interval given in each plot and are presented in Table 3. The correlation coefficient results obtained for the  $A_0$  dominated wave mode shows the detection results for damages occurring on the sensor's side of the skin are 100% higher than the ones obtained at the flip side of the skin suggesting a higher damage detection sensitivity to damages obtained at the respective sensor side.

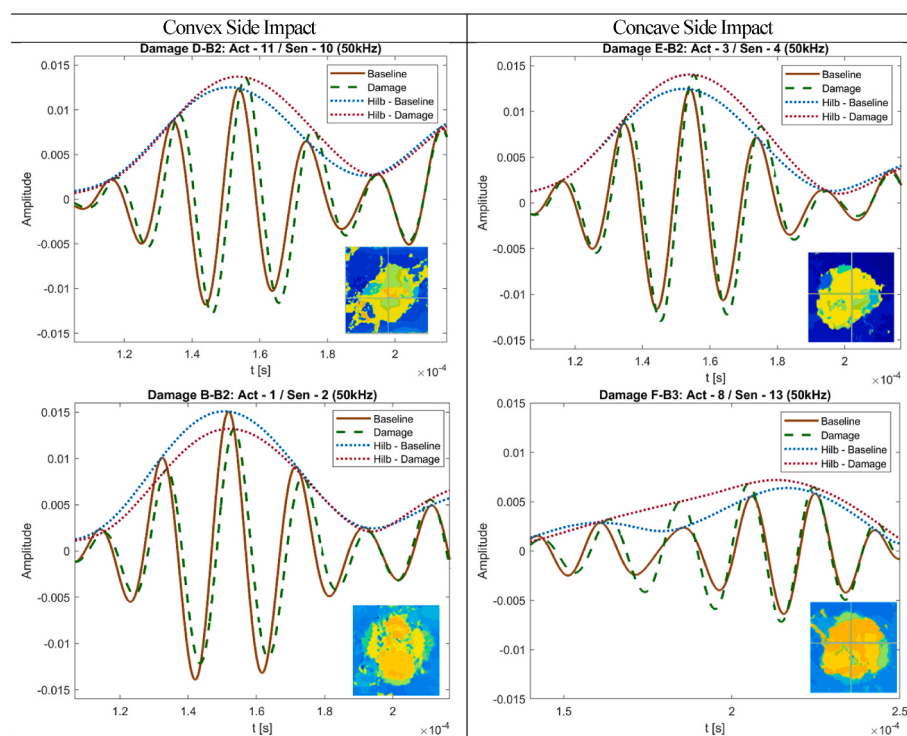


**Fig. 16.** Guided wave signal comparison for damages in the skin between sensors for both convex and concave sides.

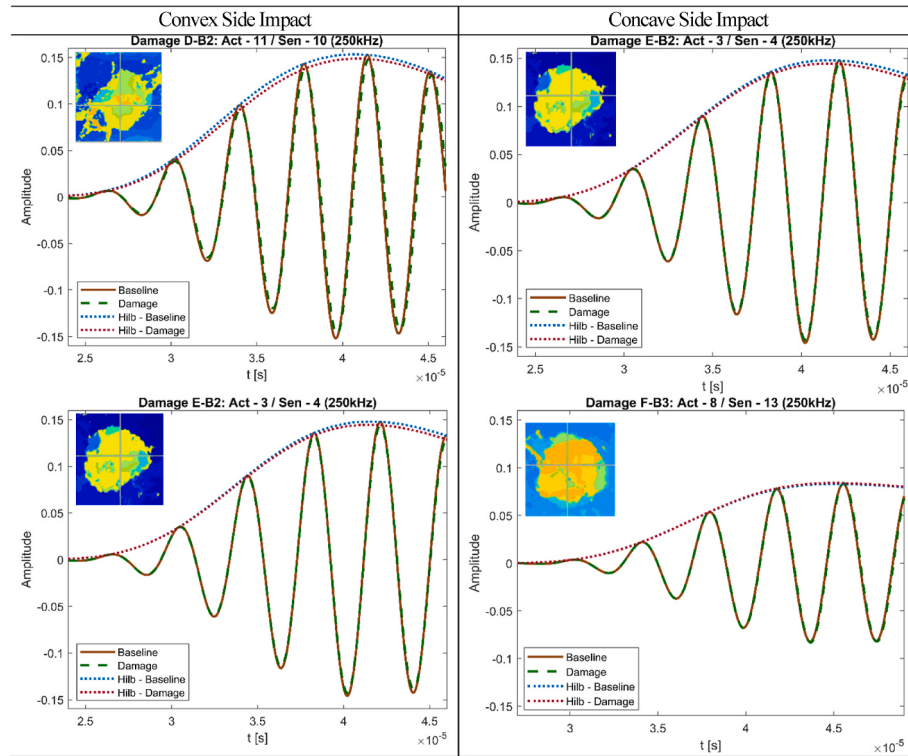


**Fig. 17.**  $S_0$  wave mode comparison for damages in the skin between sensors for both convex and concave sides.

**Table 3**

Correlation coefficient results for damages between sensors in both concave and convex sides.

ID	D-B2	B-B2	E-B2	F-B3
$DI(A_0)$	0.1639	0.1204	0.0676	0.0672
$DI(S_0)$	8.40e-03	2.76e-04	1.77e-04	1.11e-03

#### 4.4. Probability of Detection (POD)

Current SHM methodologies performance criteria rely on the calculation of the POD as a function for the flaw size [39]. Particularly, MIL-HDBK-1823 [12] recommends reporting the crack size with 90% detection probability and with a statistical confidence of 95% given by  $a_{90}$  and  $a_{90|95}$ , respectively. Here, the  $\hat{a}$  versus  $a$  approach proposed in [12] is used for calculating the POD, where  $\hat{a}$  stands for the detection metric, here given by the Mahalanobis distance between the threshold training data and the detection features, and  $a$  will here be considered as the delamination area from each independent impact. The relation between  $\hat{a}$  and  $a$  is approximated with a linear regression model [7,40], given by

$$\log(\hat{a}) = \beta_0 + \beta_1 \log(a) + \epsilon, \quad (7)$$

Where  $\beta_0$  and  $\beta_1$  are the intercept and the slope of the regression line and

**Table 4**

POD model parameters for damage categories.

Damage Category	$\beta_0$	$\beta_1$	$\tau^2$	$\hat{a}_{90}$	$\hat{a}_{90 95}$
Skin Inside	-21.71	4.53	0.26	192.84	211.88
Skin Outside	-18.87	3.85	1.02	274.86	321.98
Lip	-23.16	4.63	0.86	264.15	292.62
Stringer	-26.68	5.09	0.22	282.48	297.81

are calculated using a maximum likelihood estimation, and the error,  $\epsilon \sim \mathcal{N}(0, \tau^2)$ , are assumed independent random variables with a 0-mean normal distribution and a constant variance  $\tau^2$ .

The impacts for each damage category, detailed in Table 2, show a good distribution of damage areas. Therefore, the POD curve for each category can be computed using the each damage sizes and Mahalanobis distance to the pristine data through,

$$POD = \Phi\left(\frac{\log(a) - \hat{\mu}}{\hat{\sigma}}\right), \quad (8)$$

where  $\Phi(\bullet)$  represents the cumulative distribution function,  $\hat{\mu} = \frac{\hat{a}_{Th} - \beta_0}{\beta_1}$  for  $\hat{a}_{Th}$  being the decision threshold, computed from an inverse chi-squared distribution at 99.9% confidence. Finally,  $\hat{\sigma} = \frac{\sigma_e}{\beta_1}$ , where  $\sigma_e$  is the root mean squared error of the regression. The upper and lower confidence intervals for  $a_{90|95}$  are computed through the Wald method [39].

$$\hat{a}_{90} = \hat{\mu} + \hat{\sigma} \bullet \Phi^{-1}(0.9), \quad (9)$$

$$\hat{a}_{90|95} = \hat{a}_{90} + z_{95} \sqrt{\Gamma}, \quad (10)$$

where the second term in the sum is detailed in [39]. The model parameters,  $\beta_0$ ,  $\beta_1$ ,  $\tau^2$ ,  $\hat{a}_{90}$  and  $\hat{a}_{90|95}$  are computed for each damage category introduced in Table 2 and respectively detailed in Table 4. Additionally, the POD vs a plot [12] for each damage category are shown together in Fig. 18 with the individual  $\hat{a}_{90|95}$  values for each of the four categories are highlighted.

The  $\hat{a}_{90|95}$  values obtained for the four damage categories quantitatively describe the performance of the proposed SHM methodology for BVID detection. For a damage on the skin, the respective values for inside and outside are approximately  $212 \text{ mm}^2$  and  $322 \text{ mm}^2$ . Smaller  $\hat{a}_{90|95}$  values can be obtained due to the damage being in the sensor's direct path in the same bay. Even though these damages are imparted with the same energy and locations in the panel, the side on which they

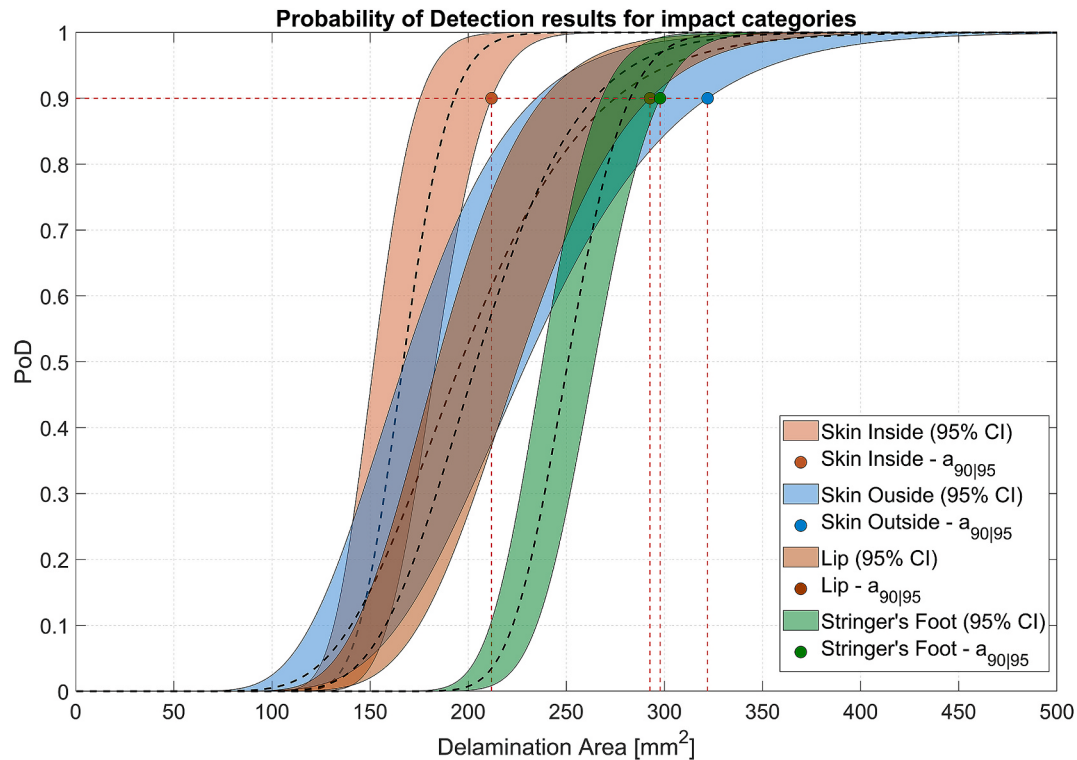


**Fig. 18.** POD vs  $a$  plots for different damage categories.

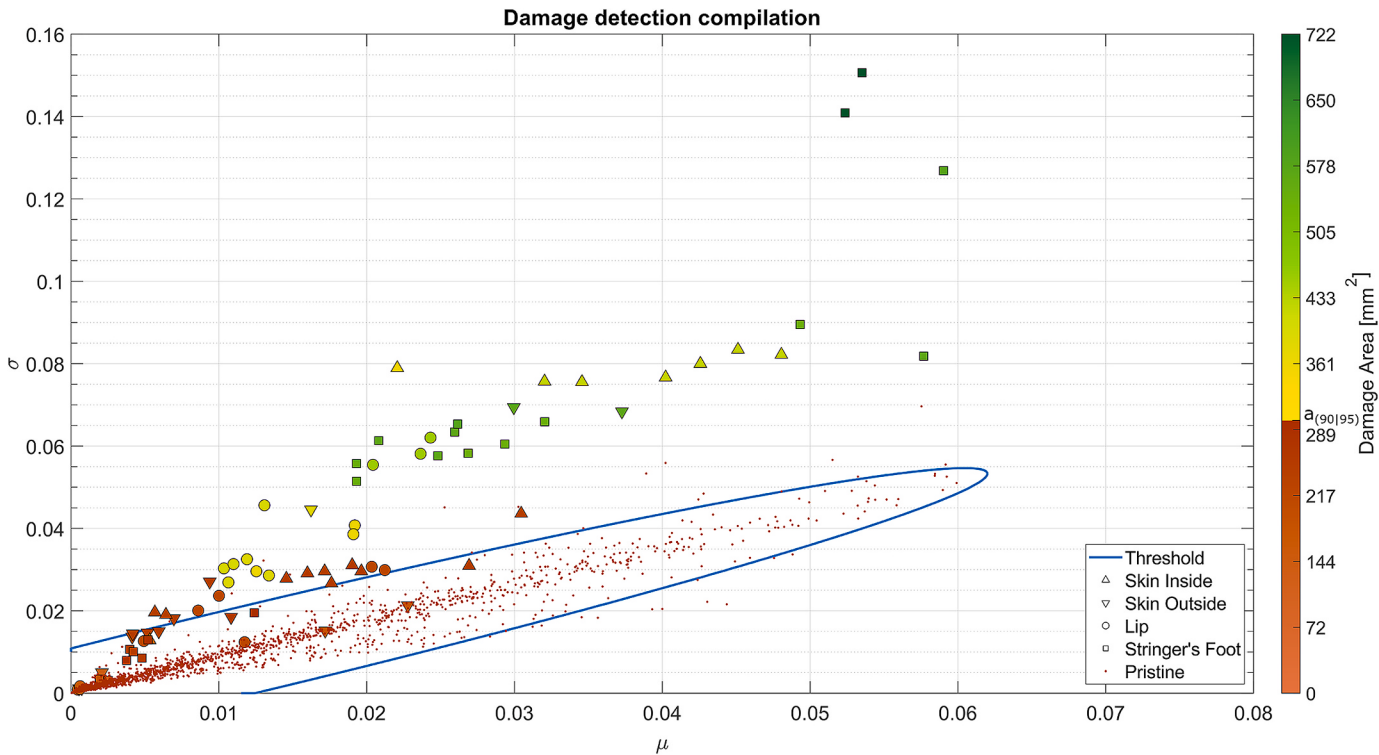


**Fig. 19.** Detection results compilation for all the damages imparted on the curved panel.

are imparted yields different results due to the positioning of the PZT sensors. Hence, a more reliable detection is obtained for the inside of the panel, for damages imparted due to tool drops [2]. For damages located away from the direct line of sight of sensors in the same bay and with

signals subjected to higher attenuation due to the presence of stringers, the  $\hat{a}_{90|95}$  values of 293 and 298 mm<sup>2</sup> are obtained for the skin-foot interface (Lip) and foot of the stringer damage categories, respectively. However, though each categories' POD curve was computed

using solely the impact data from the respective category, the worst-case scenario should be considered for categorizing the whole SHM system's reliability which corresponds to the case of the outside damages for which  $\hat{a}_{90|95} = 322 \text{ mm}^2$ , though the impacts performed in this category presented more temperature variations which can further highlight the differences between pristine and damaged stages and increases the minimum detectable damage in this category.

#### 4.5. Detection results compilation

Evaluation of the current system's POD enables the assessment of the minimum detectable damage based on the damage index features collected from the comparison from each of the signals taken prior and after each impact represented in Fig. 13 and, respectively, separated into different categories. The compilation of all detection results for these impacts is represented in Fig. 19, where the red-faced markers represent the detection results for impacts sizes under the minimum detectable size for the SHM system. Moreover, the darker-shaded markers represent damages with increasing damage sizes which overall follow the trend with increasing detection results. Previously it was reported the positive detection is assumed when the detection feature is outside the threshold which can be seen for some results below the  $\hat{a}_{90|95}$ . Often these correspond to damages in categories whose  $\hat{a}_{90|95}$  value is lower than the system's POD. Moreover, two impact results on the outside skin category are barely detected whilst having a damage below the minimum detectable size, these correspond to damage scenarios which are detected by multiple overlapping sections where, the majority of which are not able to detect this damage. This is reflected in the categories with higher associated confidence intervals obtained in the POD probabilistic distribution in Fig. 18 and highlights the uncertainty associated to performing SHM activities in larger sub-component structures.

#### 4.6. Damage localization

Once the damage presence is detected and limited to its respective sensor sub-network (here given by the local sensor groupings in Fig. 6), imaging algorithms are employed to compute the damage location by extracting features from the GW signals. Numerous localization algorithms for SHM applications have been proposed where the two predominant are the reconstruction algorithm for the probabilistic inspection of defects (RAPID), and the delay-and-sum (DAS) algorithms [2]. The first highlights the damage index only for the direct path of a transducer pair and requires a dense network of sensors to be employed for detecting the damage area. Whilst the second links the damage area to changes in the signal's properties (i.e., time of arrival and amplitude) and respective elliptical location, where the foci are the transducer pair. Recently [8], a third algorithm combining RAPID, and DAS was proposed that successfully addresses the drawbacks of both algorithms. For the RAPID algorithm, the imaging field  $I_{\text{RAPID}}(x, y)$  is given by,

$$I_{\text{RAPID}}(x, y) = \sum_{j=1}^{n_{\text{pairs}}} DI_j \frac{e - E_j(x, y)}{e - 1}, \quad (11)$$

$$E_j(x, y) = \begin{cases} 1, & \frac{d_j}{d_j(x, y)} > e \\ e, & \frac{d_j}{d_j(x, y)} < e \end{cases} \quad (12)$$

where  $e = 0.975$  [8] the ellipse's width with the sensor pair at its' foci. Here  $d_j$  and  $d_j(x, y)$  are the distance for the sensor pair  $j$ , and the Euclidian distance sum between the point at location  $(x, y)$  and the sensor pair, respectively.

$$I_{\text{DAS}}(x, y) = \frac{1}{n_{\text{pairs}}} \sum_{j=1}^{n_{\text{pairs}}} \mathcal{H}[\mathcal{B}_j(t) - \mathcal{C}_j(t)], \quad (13)$$

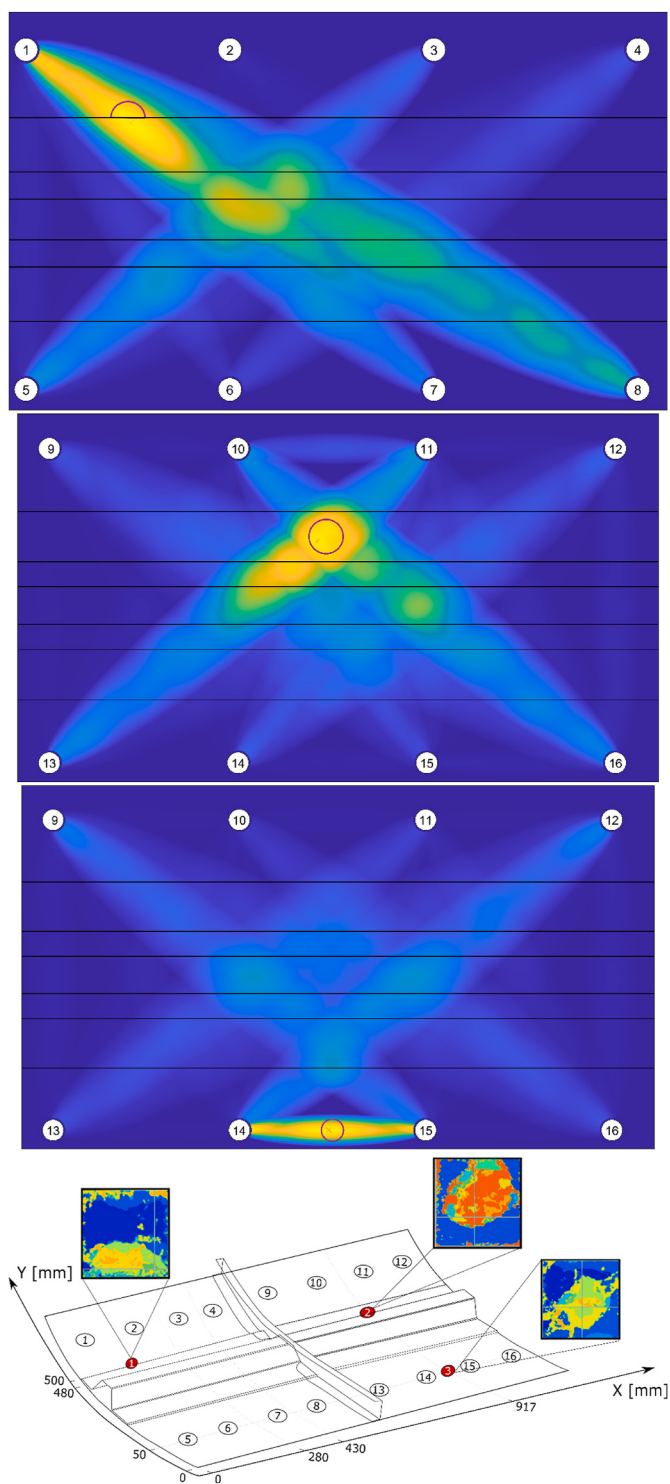


**Fig. 20.** Damage localization results for 3 different damage categories and respective panel location.

where the operator  $\mathcal{H}[\bullet]$  is the Hilbert transform, and  $\mathcal{B}_j(t) - \mathcal{C}_j(t)$  is the residual signal between the baseline and damaged state for sensor pair  $j$ , respectively. Hence, the merging between both imaging algorithms is given by  $I(x, y) = I_{\text{RAPID}}(x, y) \bullet I_{\text{DAS}}(x, y)$ .

Fig. 20 illustrates the localization results for the 3 different impact location categories and respective location in the sensor network: the skin, stringer's lip, and at the stringer's foot, where all the impacts were performed on the panel's convex side and the colormap intensity scheme

is particular to each impact. The detection true positive rate for the final impact size is 100%, meaning all the damages were fully detected and the localization step could proceed. Since the localization step should only follow once the damage presence has been confirmed and circumscribed to a given region of the network, the localization step should similarly be performed using the same 8-sensor detection grouping instead of the full network. Hence, the aforementioned localization methods were used for comparing the results for all damage locations. Analysis of this figure shows the capabilities of the current SHM system on performing localization of different impacts in locations representative of real-life scenarios on a large subcomponent structure under environmental uncertainty. Again, when group overlapping occurred, only the one presenting higher detection index to the respective threshold is presented for localization purposes.

Damage in the skin was easily detected by both algorithms, due to the reduced number of severely influenced paths, compared to the total number of sensor pair combinations. The damage at the lip of the stringer is similar to the previous, though the additional affected paths crossing the stringer were successfully highlighted by the RAPID algorithm. Furthermore, the DAS algorithm successfully distinguished the present shift in the damage location from the direct path. A second peak was obtained when combining the DAS with the RAPID algorithm, due to the lower amplitude reflections from the  $A_0$  wave mode interactions with the damage. This could be correct by employing a band filter in the results however, the full signal inspection was a more realistic approach for this methodology.

For the damage at the foot of the stringer, the DAS algorithm provides a close estimation of the actual damage location. Furthermore, when combined with the RAPID algorithm, the superposition with the direct path's influence enhances the prediction's accuracy for damages that lay in the line-of-sight between sensor pairs. This is the exact case for the damage at the foot of the stringer (Location 3), where the direct path for the sensor pairs 11–13 and 10–16 repositions the maximum localization index to the exact damage location.

## 5. Conclusion

In this work, a structural health monitoring approach using guided wave is developed at an industrial level for a complex composite fuselage panel involving different damages at different locations with different severity. The approach follows the building block approach normally adopted for manufacturing and assessment of composite parts in aircraft industry. The complete sensor network consists of an extensive sensor network employing 72 DuraAct PZT sensors connected to in-house inkjet printed circuits. The network is divided in ten overlapping groups of 16 sensors in order to maximize the amount of coverage area for damage monitoring and minimize the acquisition times.

The guided wave signal acquisition was performed using an enhanced version of an in-house LABVIEW code, which allowed controlling a maximum of 20 PZT sensors. Additional improvements to the software can be easily implemented provided similar changes are done to the controller hardware (larger RAM memory capacity and additional switch matrices). The sensor network is divided in overlapping groups of 16 sensors in order to maximize the amount of area covered for damage monitoring and minimize the signal acquisition times. However, shortcomings associated to high signal attenuation for paths over long distances and crossing structural complexities require restricting the paths being evaluated on the 16-sensor grouping. To establish a valid BB level upscaling, 3 overlapping groups of 8 sensors with similar transducer paths as the flat monostringer are chosen.

The signals for setting a reliable damage threshold were obtained through the duration of one month, yielding a total of 385 GB of data, for which the temperature fluctuations were treated as part of the environmental uncertainties given the controlled environment signals were acquired in. Damage indices relying on the Pearson's correlation coefficient were calculated for all pair-wise signal permutations on the

inspection grouping. The mean and standard-deviation of each grouping's pair-wise array is obtained, and the Outlier Analysis is applied based on the Mahalanobis distance for the temperature-wise balanced training dataset. The threshold model validation is obtained based on the false positive distribution for the testing dataset which yielded a mode of 1.5%. Uncertainties from multiple sources, including manufacturing, environmental noise, and material properties, increase the damage features when moving upwards the building block.

Once the damage threshold is set, a total of 20 impacts are imparted onto the structure at various energies (calibrated accordingly to their location in the panel). For damages in the panel's skin and at the foot of the stringer, respectively, impact energies of 25J and 35J are applied. Damages obtained from these impacts are categorized according to their specific location in the panel: skin on the inside; skin on the outside; skin-foot interface (stringer's lip); and at the foot of the stringer. The large dimensions of the panel allow for multiple damage sizes to be obtained for each respective impact (and occasional reimpacts) which are duly detected based on the previously set threshold. Sequential impacts causing the growth of the delaminations in the panel are successfully detected for signals compared between pristine and reimpact stage.

Due to the high amount of impact data provided by independent impacts on various locations of the panel, the Probability of Detection for the different damage categories is assessed and respective minimum and maximum values of  $\hat{a}_{90|95} = 212$  and  $322 \text{ mm}^2$  are obtained, respectively, for damages on the skin (inside the panel) and at the foot of the stringer.

Finally, damage examples for impacts on the skin (inside), skin-foot interface (lip) and foot of the stringer are localized through an imaging algorithm by over positioning two widely employed imaging methods for damage localization yielding accurate location results compared to the real location in the panel.

## Author statement

Francisco de Sá Rodrigues: Methodology, Software, Investigation, Data Curation, Writing - Original Draft, Writing - Review & Editing.

Ilias Giannakeas: Methodology, Software, Supervision, Writing - Review & Editing.

Zahra Sharif Khodaei: Conceptualization, Methodology, Supervision, Writing - Review & Editing, Funding acquisition.

Ferri Aliabadi: Conceptualization, Methodology, Supervision, Writing - Review & Editing, Funding acquisition.

## Declaration of competing interest

The authors declare that they have no known competing financial interests or personal relationships that could have appeared to influence the work reported in this paper.

## Data availability

The authors do not have permission to share data.

## Acknowledgments

The research leading to these results has gratefully received funding from the European JTI-CleanSky2 program under the Grant Agreement no. 314768 for SHERLOC project ([sherloc-project.com](http://sherloc-project.com)). SHERLOC project is coordinated by SI&HM group at imperial college ([www.imperial.ac.uk/structural-integrity-health-monitoring](http://www.imperial.ac.uk/structural-integrity-health-monitoring)) and lead by Leonardo S.p.A, as Topic Manager. The authors would like to acknowledge FIDAM for manufacturing of the panels and Element Seville for testing the large-scale sub-components.

## References

- [1] Rana S, Fangueiro R. Advanced composites in aerospace engineering. In: Advanced composite Materials for Aerospace Engineering; 2016.
- [2] M. F. Aliabadi and Z. S. Khodaei, Structural health monitoring for advanced composite structures. 20178..
- [3] Hussain N. Structural health monitoring and its role in affordability. In: 10th international workshop on structural health monitoring; 2015.
- [4] Speckmann H, Henrich R. Structural health monitoring (SHM). In: IMRBPP meeting. Cologne: EASA; 2007.
- [5] Goossens S, et al. A global assessment of barely visible impact damage for CFRP sub-components with FBG-based sensors. Compos Struct 2021;272:114025.
- [6] Mitra M, Gopalakrishnan S. Guided wave based structural health monitoring: a review. Smart Mater Struct 2016;25(5):053001.
- [7] Giannakeas IN, Khodaei ZS, Aliabadi MH. Digital clone testing platform for the assessment of SHM systems under uncertainty. Mech Syst Signal Process 2022;163:108150.
- [8] Yue N, Khodaei ZS, Aliabadi MH. Damage detection in large composite stiffened panels based on a novel SHM building block philosophy. Smart Mater Struct 2021; 30(4):045004.
- [9] Michaels JE. Detection, localization and characterization of damage in plates with an in situ array of spatially distributed ultrasonic sensors. Smart Mater Struct 2008; 17(3):035035.
- [10] Yan G. A Bayesian approach for damage localization in plate-like structures using Lamb waves. Smart Mater Struct 2013;22(3):035012.
- [11] Marzani A, et al. Implementation of a structural health monitoring system for a composite wing box skin. In: Smart intelligent aircraft structures (SARISTU) proceedings of the final project conference; 2016.
- [12] Amse N, Hifac AA. Department of defense handbook. 1998.
- [13] Falsetelli F, et al. Probability of detection, localization, and sizing: the evolution of reliability metrics in Structural Health Monitoring. Struct Health Monit 2022;21 (6):2990–3017.
- [14] Aldrin JC, et al. Demonstration study for reliability assessment of SHM systems incorporating model-assisted probability of detection approach. AIP Conference Proceedings; 2012.
- [15] Wölcken PC, Papadopoulos M. Smart intelligent aircraft structures (SARISTU): proceedings of the final project conference. 2015.
- [16] Salmanpour MS, Sharif Khodaei Z, Aliabadi MF. Impact damage localisation with piezoelectric sensors under operational and environmental conditions. Sensors 2017;17(5):1178.
- [17] Bekas DG, Sharif-Khodaei Z, Aliabadi MF. An innovative diagnostic film for structural health monitoring of metallic and composite structures. Sensors 2018;18 (7):2084.
- [18] Bekas DG, et al. Quality assessment and damage detection in nanomodified adhesively-bonded composite joints using inkjet-printed interdigital sensors. Compos Struct 2019;211:557–63.
- [19] Feng T, Aliabadi MF. Structural integrity assessment of composites plates with embedded PZT transducers for structural health monitoring. Materials 2021;14 (20):6148.
- [20] Giannakeas IN, Khodaei ZS, Aliabadi MF. Structural health monitoring cost estimation of a piezosensorized aircraft fuselage. Sensors 2022;22(5):1771.
- [21] Yue N, Sharif Khodaei Z, Aliabadi MH. An innovative secondary bonding of sensors to composite structures for SHM application. In: Key engineering materials; 2018.
- [22] Mei H, Giurgiu V. Guided wave excitation and propagation in damped composite plates. Struct Health Monit 2019;18(3):690–714.
- [23] Sharif-Khodaei Z, Ghajari M, Aliabadi MH. Impact damage detection in composite plates using a self-diagnostic electro-mechanical impedance-based structural health monitoring system. J Multiscale Model (JMM) 2015;6(4):1550013.
- [24] Lambinet F, Khodaei ZS. Measurement platform for structural health monitoring application of large scale structures. Measurement 2022;190:110675.
- [25] Rodrigues FdS, et al. Structural health monitoring platform for industrial scale composite structures. AIP Conf Proc 2023.
- [26] Michaels JE, et al. Chirp excitation of ultrasonic guided waves. Ultrasonics 2013;53 (1):265–70.
- [27] Rizzo P, di Scalea FL. Feature extraction for defect detection in strands by guided ultrasonic waves. Struct Health Monit 2006;5(3):297–308.
- [28] Giannakeas IN, Sharif Khodaei Z, Aliabadi MH. An up-scaling temperature compensation framework for guided wave-based structural health monitoring in large composite structures. Struct Health Monit 2023;22(2):777–98.
- [29] Guo N, Cawley P. The interaction of Lamb waves with delaminations in composite laminates. J Acoust Soc Am 1993;94(4):2240–6.
- [30] Ng C, Veidt M. Scattering of the fundamental anti-symmetric Lamb wave at delaminations in composite laminates. J Acoust Soc Am 2011;129(3):1288–96.
- [31] Chua CA, Cawley P. Crack growth monitoring using fundamental shear horizontal guided waves. Struct Health Monit 2020;19(5):1311–22.
- [32] Gazis DC. Three-dimensional investigation of the propagation of waves in hollow circular cylinders. I. Analytical foundation. J Acoust Soc Am 1959;31(5):568–73.
- [33] Gazis DC. Three-dimensional investigation of the propagation of waves in hollow circular cylinders. II. Numerical results. J Acoust Soc Am 1959;31(5):573–8.
- [34] Nishino H, et al. Modal analysis of hollow cylindrical guided waves and applications. Jpn J Appl Phys 2001;40(1R):364.
- [35] Ricci F, et al. Guided waves in a stiffened composite laminate with a delamination. Struct Health Monit 2016;15(3):351–8.
- [36] Flynn EB, et al. Maximum-likelihood estimation of damage location in guided-wave structural health monitoring. Proc R Soc A 2011;467(2133):2575–96.
- [37] Rose JL. The semi-analytical finite element method. Ultrasonic Guided Waves in Solid Media 2014:135–54.
- [38] () Model 086D20. Short-sledge Impulse Hammer w/force sensor & tips, 0 to 5k lbf, 1 mV/lbf. Available: [https://www.pcb.com/contentstore/docs/PCB\\_Corporate/Vibration/products/Manuals/086D20.pdf](https://www.pcb.com/contentstore/docs/PCB_Corporate/Vibration/products/Manuals/086D20.pdf).
- [39] Schubert Kabban CM, et al. The probability of detection for structural health monitoring systems: repeated measures data. Struct Health Monit 2015;14(3): 252–64.
- [40] Moriot J, et al. A model-based approach for statistical assessment of detection and localization performance of guided wave-based imaging techniques. Struct Health Monit 2018;17(6):1460–72.